ADVANCED MATERIALS

Supporting Information

A Metal-Like Conductive Elastomer with a Hierarchical Wrinkled Structure

Seokmin Lee, Yongkwon Song, Yongmin Ko, Younji Ko, Jongkuk Ko, Cheong Hoon Kwon, June Huh, Sang-Woo Kim, Bongjun Yeom,* and Jinhan Cho*

Supporting Information

Metal-like Conductive Elastomer with Hierarchical Wrinkled Structure

Seokmin Lee, Yongkwon Song, Yongmin Ko, Younji, Ko, Jongkuk Ko, Cheong Hoon Kwon, June Huh, Sang-Woo Kim, Bongjun Yeom[*], and Jinhan Cho*

Supporting materials include:

Experimental Section

Figure S1. Synthesized TB-Au NPs.

Figure S2. FTIR spectra of TB-Au NP and TA.

Figure S3. FE-SEM images of (TB-Au NP/diethylenetriamine (DA))$_n$ multilayers.

Figure S4. FE-SEM images of (TB-Au NP/poly(ethylene imine) (PEI))$_n$ multilayers.

Figure S5. Schematic representation of laser diffraction and diffraction intensity analysis.

Figure S6. Surface morphology of (TB-Au NP/TA)$_n$ multilayers.

Figure S7. FE-SEM images of (TB-Au NP/TA)$_1$ -coated PDMS and its cross-sectional profile.

Figure S8. Film thickness of (TB-Au NP/TA)$_n$ multilayers.

Figure S9. Surface morphology of (anionic citrate-Au NP /TA)$_n$ multilayers.

Figure S10. Modulus calculation of (TB-Au NP/TA) on PDMS.

Figure S11. Stress-strain curves for PDMS and (TB-Au NP/TA)$_{15}$ multilayer-coated PDMS.

Figure S12. Charge transport mechanism of (TB-Au NP/TA)$_n$ multilayers.

Figure S13. Resistance change of (TB-Au NP/TA)$_n$-coated PDMS as function of cycle number.

Figure S14. Electrical stability of the wrinkled elastomeric electrode under various deformation..

Figure S15. Resistance of a helical-structured PDMS electrode.

Figure S16. Preparation of PDMS electrodes with intaglio and embossed structures.

Figure S17. Photographic images of the (TB-Au NP/TA)$_2$ coated on curve shaped PDMS

Figure S18. FE-SEM image of (TB-Au NP/TA)$_{15}$-PDMS after 100 peeling cycles

Figure S19. Schematic representation of the triboelectric mechanism of TENGs.

Figure S20. Triboelectric measurement of (TB-Au NP/TA)$_n$ multilayer-based TENG devices.

Figure S21. Output voltages of TENG.

Figure S22. LEDs illuminated by all elastomer-based TENG.

Figure S23. Triboelectric potential distribution in the different TENG electrodes.

Figure S24. Electric output of TENGs as a function of external resistance.

Figure S25. LEDs illuminated by all-elastomer-based TENGs using finger force.

Other Supplementary Materials for this manuscript includes the following:
Movie S1 (.mov format) Lighting LED while stretching the electrode

Movie S2 (.mov format) Electrode peeling test

Movie S3 (.mov format) All-elastomer based TENG

Movie S4 (.mov format) Lighting 30 LEDs by tapping

Experimental Section

Materials

Poly(dimethylsiloxane) (Sylgard 184) and tetraoctylammonium bromide (TB) were purchased from Dow Corning, and Alfa Aesar, respectively. Gold(III) chloride trihydrate ($HAuCl_4 \cdot 3H_2O$), sodium borohydride ($NaBH_4$), tris-(2-aminoethyl)amine (TA), and (3-mecaptopropyl) trimethoxysilane were purchased from Sigma Aldrich. The more detailed explanation about experimental process is given in Supplementary Information.

Synthesis of tetraoctylammonium bromide-stabilized Au NPs

TB-stabilized Au NPs with a diameter of approximately 7 ± 3 nm were synthesized in toluene and added to a 25 mM solution of TB in toluene (80 mL). The transfer of the metal salt to the toluene phase could be clearly observed within a few seconds. A freshly prepared 0.4 M solution of $NaBH_4$ (25 mL) was added to the stirred mixture, which caused immediate reduction. After 30 min, the two phases were separated, and the toluene phase was subsequently washed with 0.1 M H_2SO_4, 0.1 M NaOH, and H_2O (three times).

Preparation of thiol-functionalized PDMS film

For the preparation of SH-PDMS films, we first prepared a PDMS prepolymer mixture (base: cross-linking curing agent = 10:1, w/w). Bubbles formed from the PDMS prepolymer mixture were removed in a vacuum chamber for 30 minutes. The doctor-blade process was then used after pouring the PDMS prepolymer mixture onto a fluorosilanized Si-wafer. The prepolymer mixture was cured at 150 °C for 15 minutes and peeled off from the wafer. After curing, the PDMS films were thiolated as described by Brook and co-workers.[S1]. In brief, the PDMS films were dipped into a mixture of 2.65 mL of (3-mecaptopropyl) trimethoxysilane and 28 mL of methanol solution containing 2.8 g of KOH for 6 hours at 50 °C with sonication and

then washed with dichloromethane.

Preparation of multilayer electrodes

TB-Au NPs in toluene (5 mg mL^{-1}) and TA in ethanol (1 mg mL^{-1}) were deposited alternately onto substrates (quartz glass or SH-PDMS) using LbL assembly with a dipping time of 30 min. First, a quartz glass substrate was chemically treated in RCA solution (H$_2$O: H$_2$O$_2$: NH$_4$OH = 5: 1: 1 (volume ratio)), then dipped into the TA solution for 30 minutes, and finally washed with pure ethanol to remove the weakly adsorbed TA molecules. Subsequently, the TA-coated substrate was immersed into the hydrophobic NP solution for 30 min and then washed with pure toluene, resulting in a one-bilayer film. Elastomeric electrodes were prepared by dipping a SH-PDMS substrate in TB-Au NP solution and then washing with pure toluene. After coating TB-Au NPs onto the SH-PDMS substrate, the substrate was dipped into the TA solution. These procedures were repeated to form multilayers with the desired thickness or bilayer number (*n*) (i.e., (TB-Au NP/TA)$_n$ multilayers).

Characterization of (TB-Au NP/TA)$_n$ multilayers

Fourier transform infrared (FTIR) spectra of the multilayers were collected using a CARY 600 spectrometer (Agilent Technology) in specular mode with a resolution of 4 cm^{-1}, and the obtained data were plotted using spectrum analysis software (OMNIC, Nicolet). FE-SEM and EDX were conducted using an S-4800 microscope (Hitachi). High-resolution transmission electron microscopy (HR-TEM) of synthesized TB-Au NPs was conducted using a Tecnai20 microscope (FEI). A green laser (λ = 532 nm) was used to obtain light diffraction patterns. The green laser beam was incident to the wrinkled surface, and the light diffraction patterns on the screen (the distance between the sample and the screen was 10 cm) were obtained. The surface morphology of the formed multilayers was scanned using atomic force microscopy (AFM, XE-100, Park systems) in tapping mode. The temperature dependence of the electrical

conductivity of the formed multilayers was measured using a physical property measurement system (PPMS-9, Quantum Design) over a temperature range from 2 to 300 K. Error bars in electrical properties of the multilayers represent the standard deviation of each value obtained from three samples.

Molecular dynamics simulations

All-atom molecular dynamics (MD) simulations were performed for a model system consisting of TA molecules between Au (100) surfaces. The initial molecular geometries were prepared by placing *n* TA molecules between Au slabs built by face-centered-cubic (FCC) stacking with a (100) face consisting of a 7×7 supercell. With this system constitution, NPT-ensemble MD simulations were carried out using a Forcite module with a COMPASS force field[S2] (COMPASS II) as implemented in the Material Studio package. The Nosé–Hoover–Langevin thermostat[S3] and Parrinello–Rahman barostat[S4] were used for maintaining temperature (298 K) and pressure (1 bar), respectively. For all NPT MD runs, the electrostatic potential energy was calculated by the Ewald summation method with an accuracy of 0.1 kcal/mol and a buffer width of 0.5 Å, and the van der Waals potential energy was calculated by the atom-based technique with a cutoff distance of 12.5 Å and a spline width of 1 Å. The MD system was equilibrated for 5 ns with a time step of 1 fs.

Measurement of electrical properties of the wrinkled elastomeric electrode

Before measuring the electrical properties, four edges of the elastomeric electrode were cut to measure only one side of the electrode. The electrical conductivity was calculated from the sheet resistance measured using a four-point probe (MCP-T610, Mitsubishi Chemical Analytech) and the thickness of the (TB-Au NP/TA)$_n$ film measured from cross-sectional FE-SEM images. The electrical conductivity under different strains was measured using a two-point probe (Keithley 4200-SCS).

Measurements of TENGs

A pushing tester (LabWorks, Inc., model ET-126–1) was used to apply a vertical compressive force to the TENGs with a distance of 1 cm between the elastomeric electrode and PDMS plate (contact area of 1.5 cm × 1.5 cm). A Tektronix DMO 3052 digital oscilloscope and a low-noise current preamplifier (Stanford Research Systems, Inc., model SR570) were used for the open-circuit output voltage and short-circuit output current, respectively
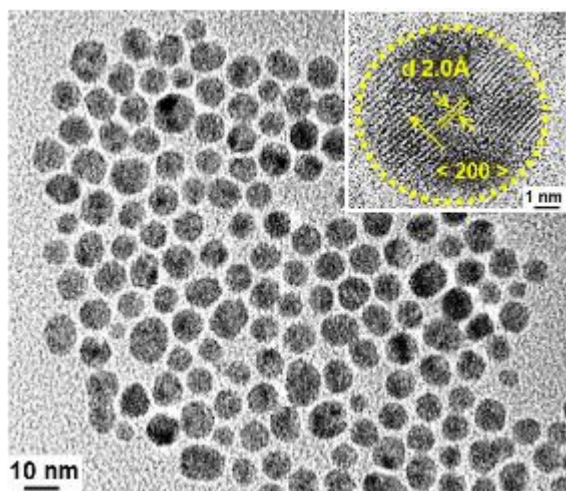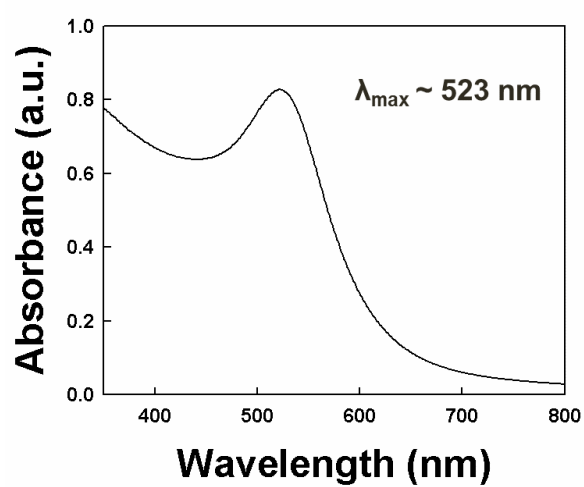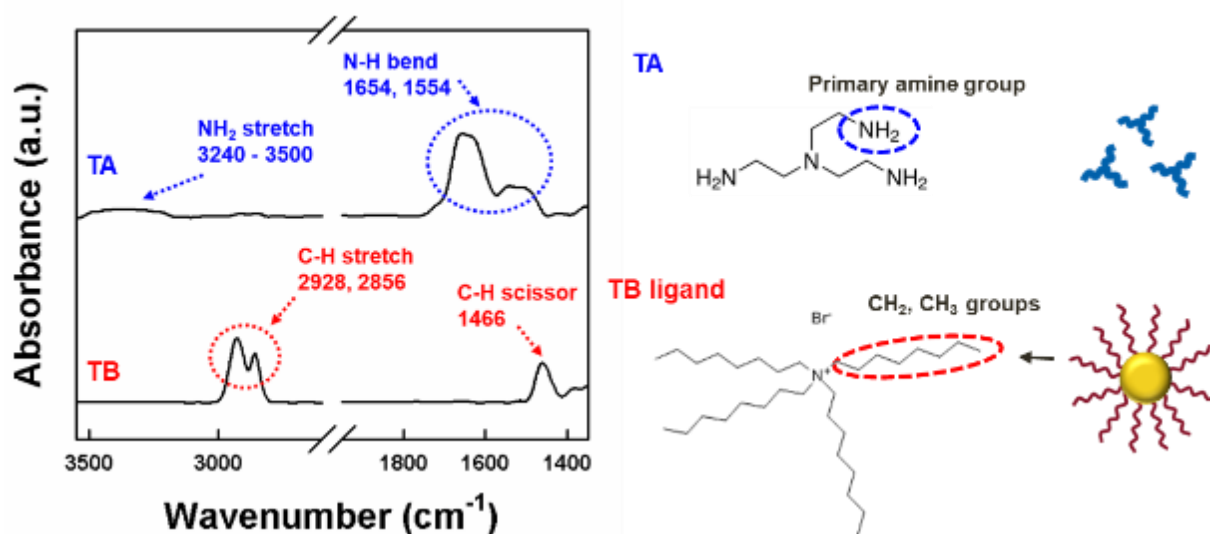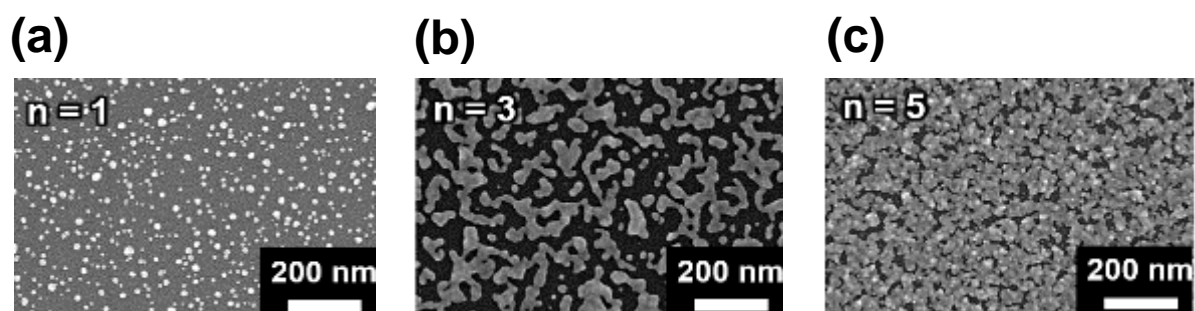
Figure S1. a) High-resolution transmission electron microscopy image b) UV-vis spectrum of TB-Au NPs synthesized in toluene.

Figure S2. FTIR spectra of TB-Au NP and TA. Characteristic FTIR spectra of native TB ligands, which have bulky long alkyl chains, and TA, which comprises three amine groups.

Figure S3. FE-SEM images of (TB-Au NP/diethylenetriamine (DA))$_n$ multilayers with n = (a) 1, (b) 3, and (b) 5. These multilayers were deposited onto Si wafers. Additionally, the molecular weight (M$_w$) of the used DA was 104.

(a)

(b)
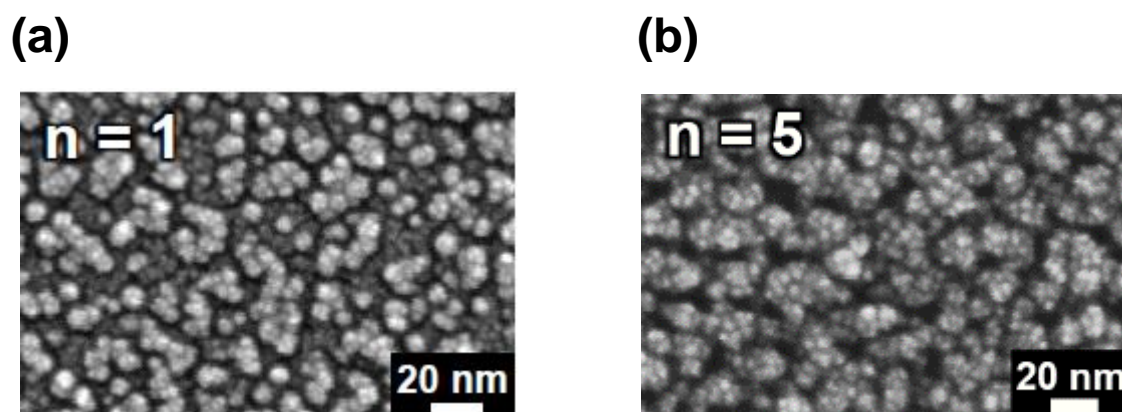
Figure S4. FE-SEM images of (TB-Au NP/poly(ethylene imine) (PEI))$_n$ multilayers with n = (a) 1 and (b) 5. These multilayers were deposited onto Si wafers. Additionally, the molecular weight (M$_w$) of the used PEI was 50,000.
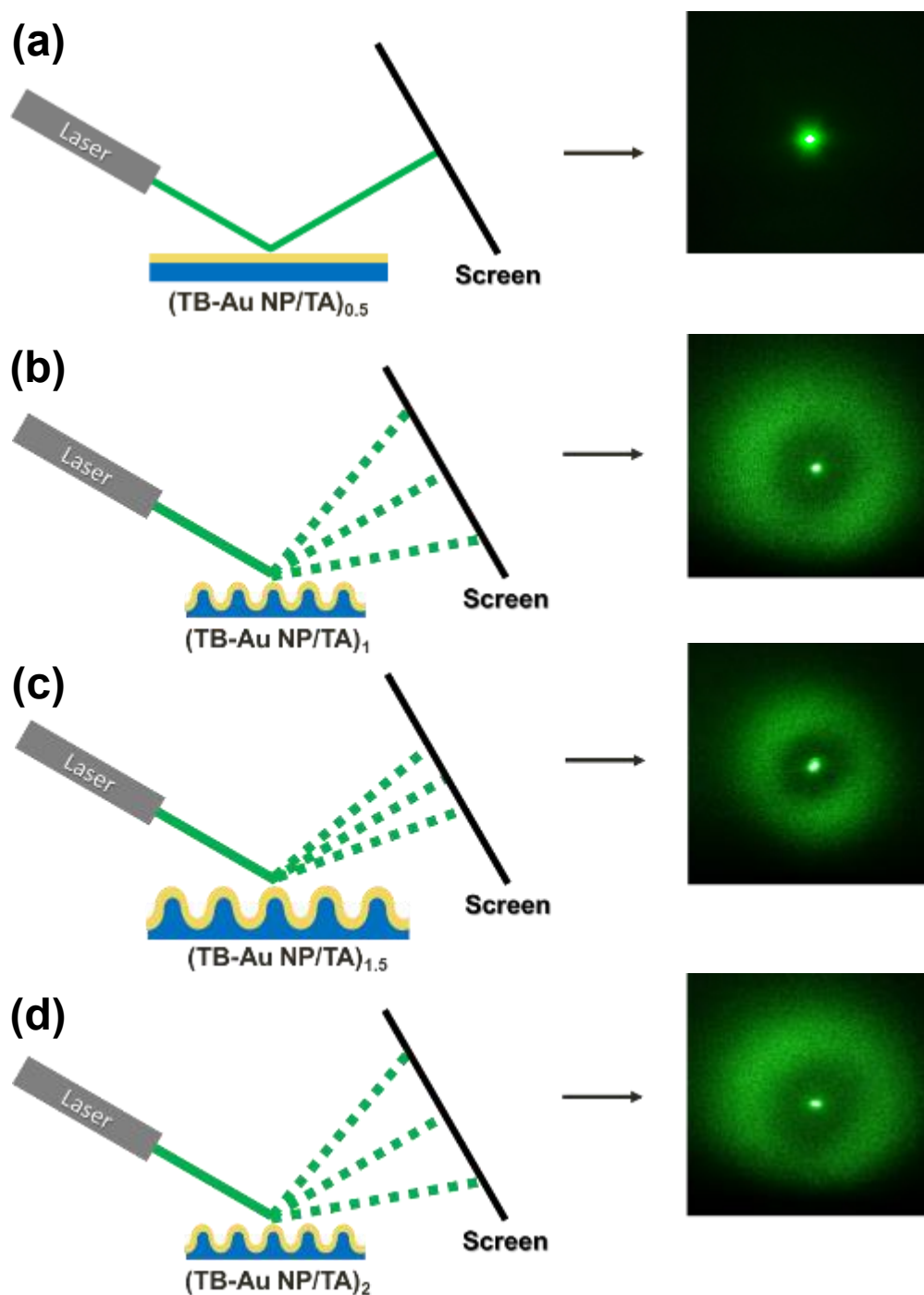
Figure S5. Schematic representation of laser diffraction and diffraction intensity analysis**.** A green laser beam ($\lambda = 532$ nm) was incident to (TB-Au NP/TA)$_n$-coated PDMS films with $n =$ 0.5, 1, 1.5, and 2. The distance between the wrinkled sample and the screen was 10 cm.
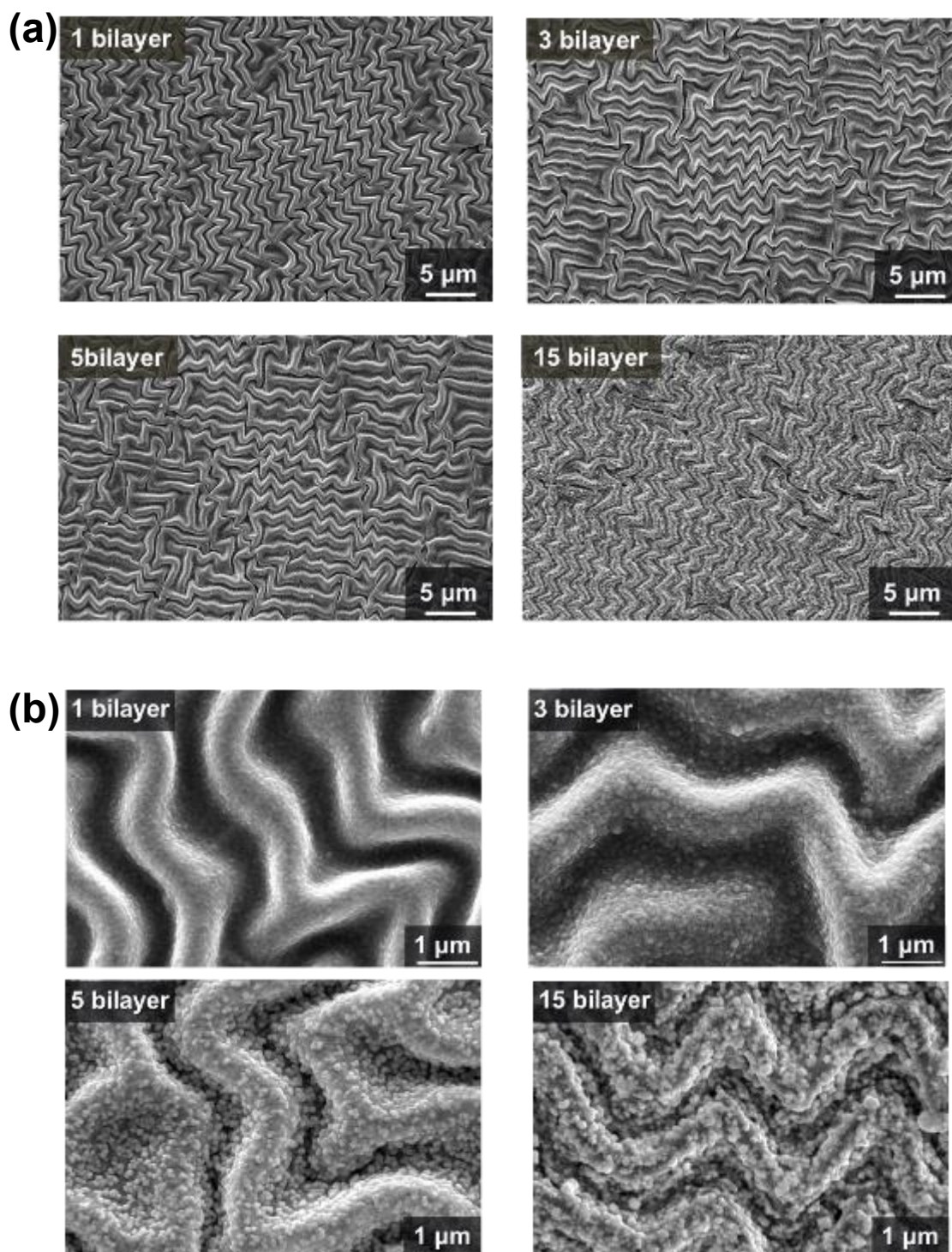
Figure S6. Surface morphology of (TB-Au NP/TA)$_n$ multilayers. FE-SEM images of (TB-Au NP/TA)$_n$ multilayers with n = 1, 3, 5, and 15 on PDMS substrates. The wavelengths of surface wrinkles were almost fixed at approximately 1.6 μm for all bilayer numbers.
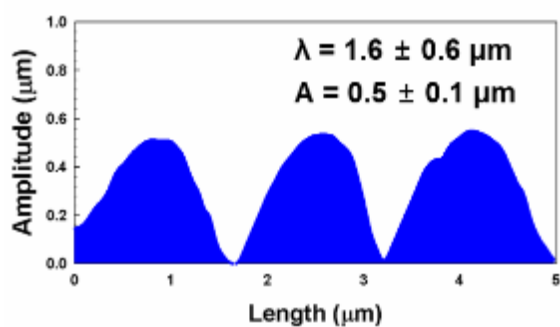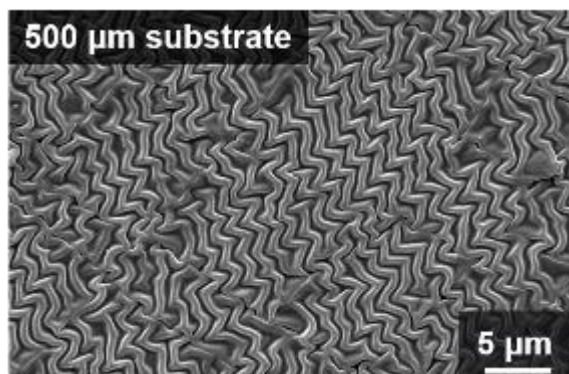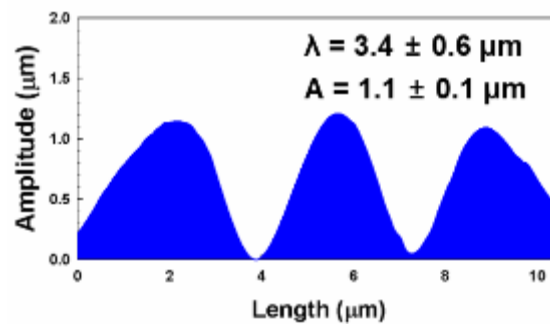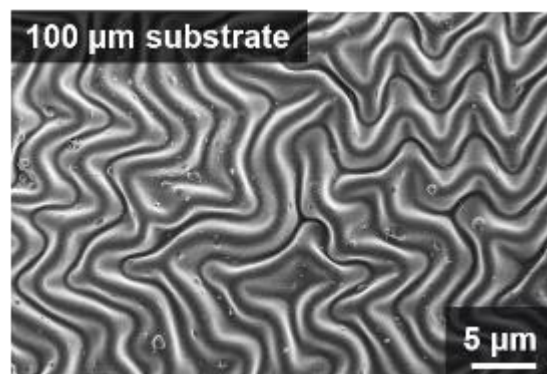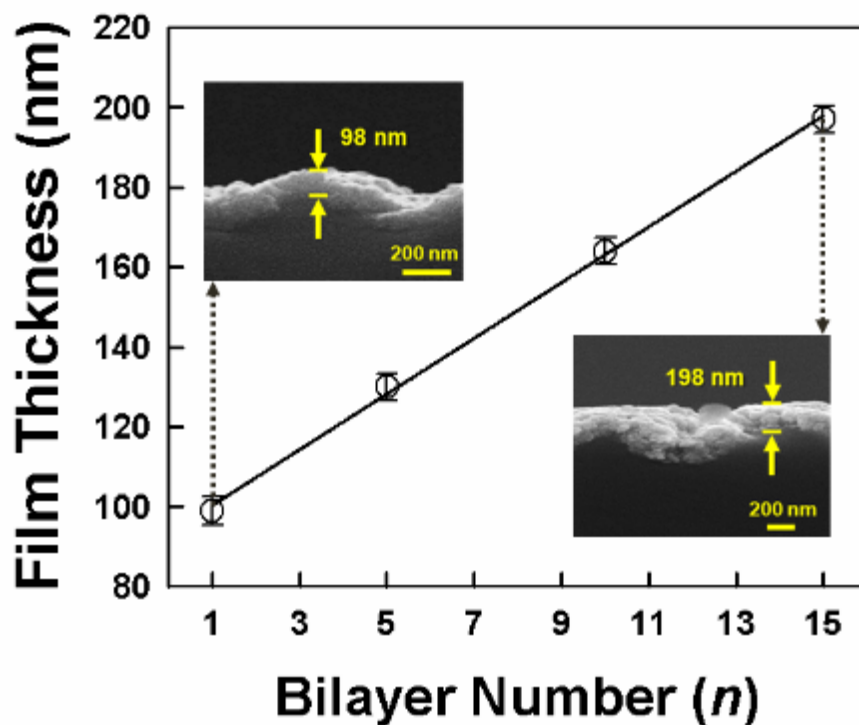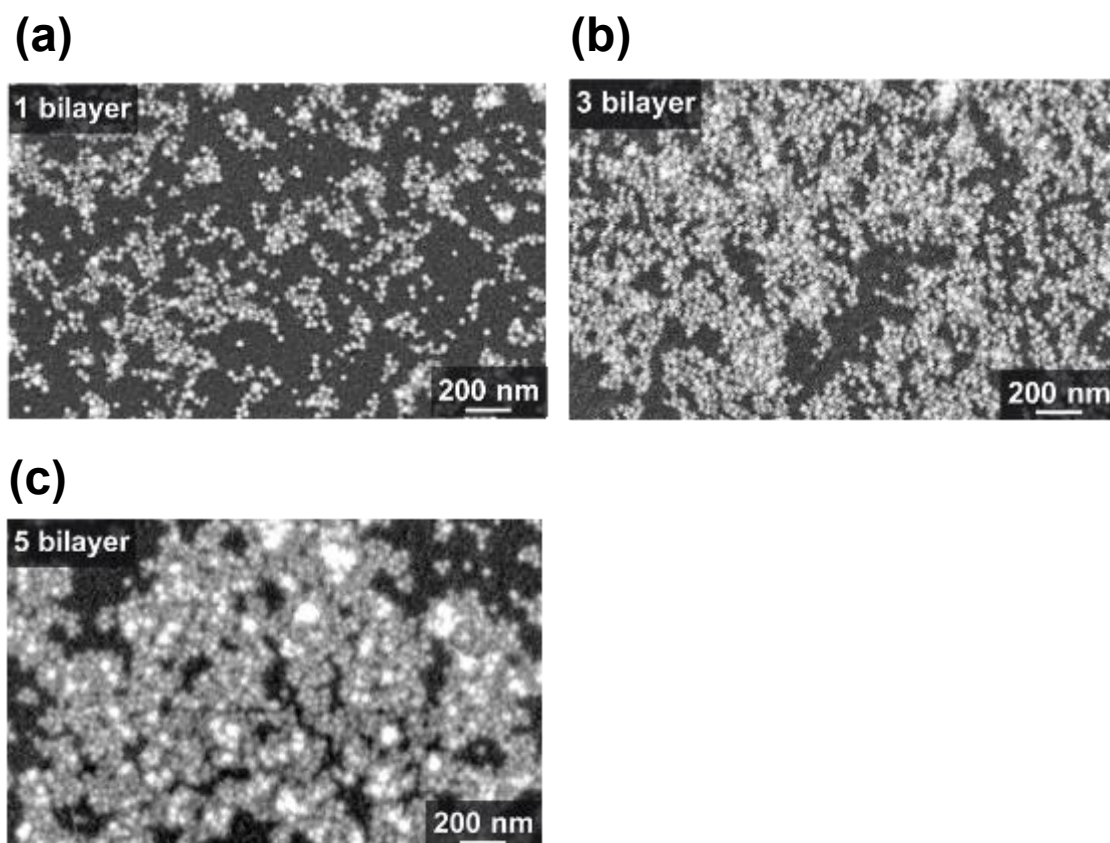
Figure S7. FE-SEM images of (TB-Au NP/TA)₁ multilayer-coated PDMS and its cross-sectional profile showing the wavelength and amplitude of the wrinkled structures. In this case, thicknesses of the used PDMS substrates were (a) 500 and (b) 100 μm.

**Figure S8.** Film thickness of (TB-Au NP/TA)$_n$ multilayers. Film thickness of (TB-Au NP/TA)$_n$ multilayers with increasing bilayer number from 1 to 15. The inset shows the cross-sectional FE-SEM images of (TB-Au NP/TA)$_n$ multilayers. The thickness of one (TB-Au NP/TA) bilayer on SH-PDMS was approximately 98 nm. As the number of bilayers was increased, the bilayer thickness of approximately 7.1 nm increased. The bilayer thickness was almost the same as the diameter of the TB-Au NPs.

WILEY-VCH

(a)

(b)

(c)

Figure S9. Surface morphology of (anionic citrate-Au NP /TA)$_n$ multilayers. FE-SEM images of (anionic citrate-Au NP /TA)$_n$ multilayers with n = 1, 3, and 5 on a Si-wafer. In this case, anionic Au NPs preserved their shape and size without any partial metallic fusion at room temperature. Anionic citrate ion-stabilized Au NPs with a diameter of approximately 12 nm were synthesized as follows: 0.85 mM HAuCl$_4$ was added to 100 mL of a 1 mg·mL^{-1} citrate aqueous solution. After vigorous stirring, 1 mL of 74 mM NaBH$_4$ was subsequently added to the mixture. The resultant anionic Au NP solution was adjusted to pH 4.5 by the addition of 0.1 M HCl.
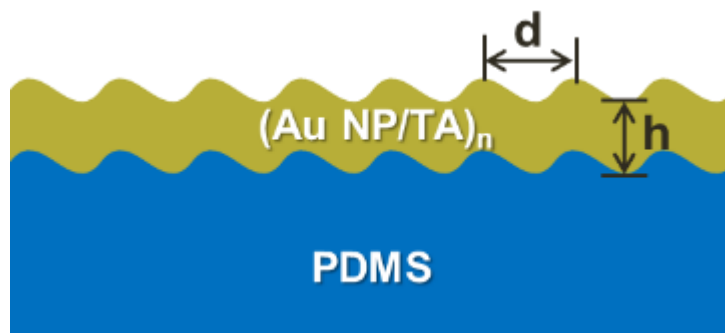
Figure S10. Modulus calculation of (TB-Au NP/TA) on PDMS**.** Schematic representation of the (TB-Au NP/TA)$_n$-coated PDMS film. Here, *d* and *h* represent the wavelength of the wrinkle pattern and the thickness of the (TB-Au NP/TA) layer, respectively. The plane-strain modulus of (TB-Au NP/TA) on PDMS was calculated with equation S1:

$$\overline{E_f} = \frac{3E_s}{(1 - v_s^2)} \left(\frac{d}{2\pi h}\right)^3 \quad (S1)$$

where *E* is the Young's modulus, and *v* is the Poisson's ratio. The subscripts f and s refer to (TB-Au NP/TA) and PDMS, respectively. The parameters are as follows: E_s = 1.8 MPa, v_s = 0.4, *d* = 1.6 μm, and *h* = 98 nm. Equation (S1) yields an estimated plane-strain modulus of 113 MPa. The modulus calculation was only conducted with a 1-bilayer sample, because the wavelength (1.6 μm) is independent of bilayer number, and because the thickness increases with bilayer number.
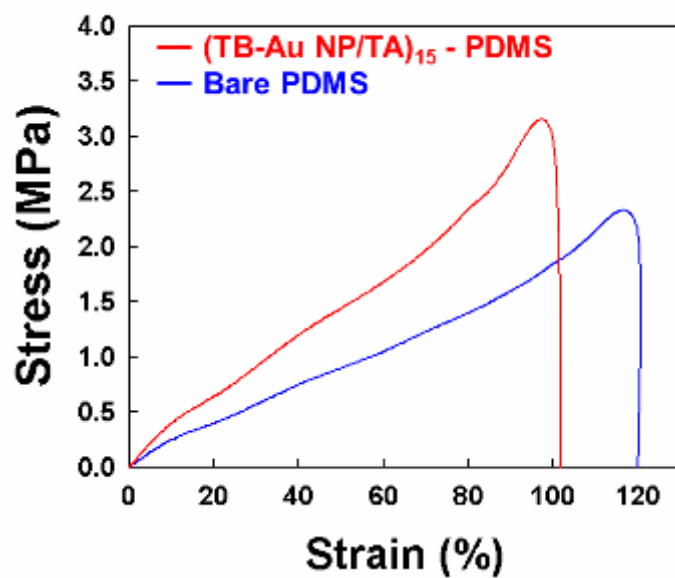
Figure S11. Stress-strain curves for bare PDMS and (TB-Au NP/TA)$_{15}$ multilayer-coated PDMS.

(a)

(b)
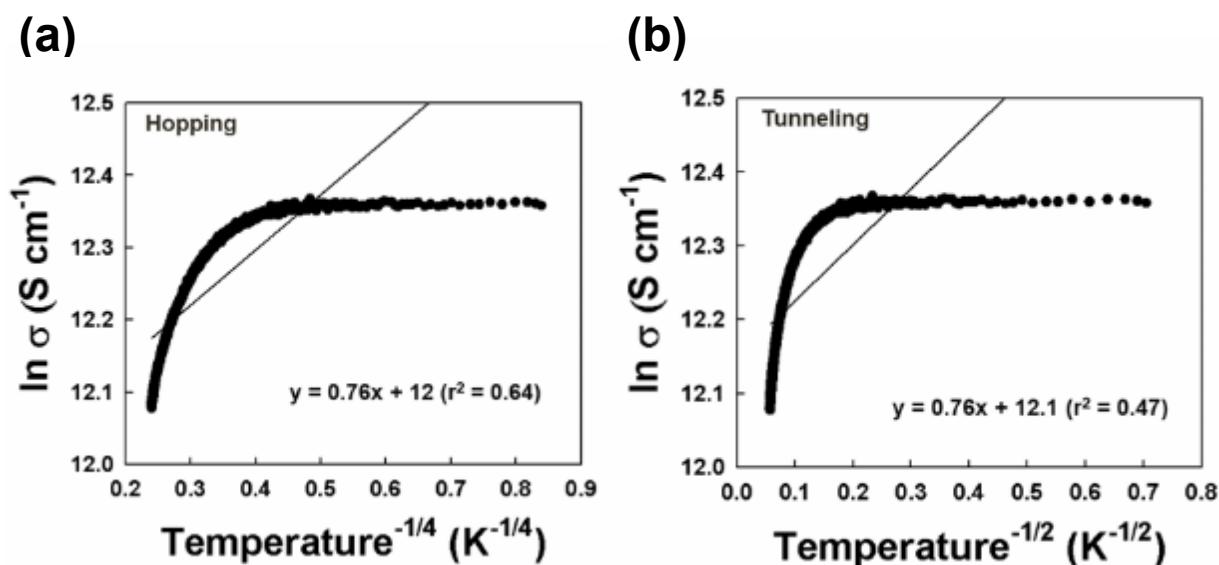
Figure S12. Charge transport mechanism of (TB-Au NP/TA)$_n$ multilayers. a) Plot of lnσ vs $T^{-1/4}$ for the hopping mechanism. b) Plot of lnσ vs $T^{-1/2}$ for the tunneling mechanism of the (TA/TB-Au NP)$_{30.5}$ multilayer films. The electron transport mechanism for semiconductors can be demonstrated by the various-range hopping and tunneling conduction processes as follows: $\sigma = \sigma_0 \exp(-A/T^{(1/d+1)})$, where σ is the conductivity, T is the absolute temperature (K), A is a constant, and d is the dimensionality. The conductivity (lnσ) as a function of $T^{-1/4}$ (for hopping) or $T^{-1/2}$ (for tunneling) for (TB-Au NP/TA)$_{15}$ does not have a linear dependence, suggesting metallic conduction behavior rather than hopping or tunneling conduction behavior between adjacent Au NPs.
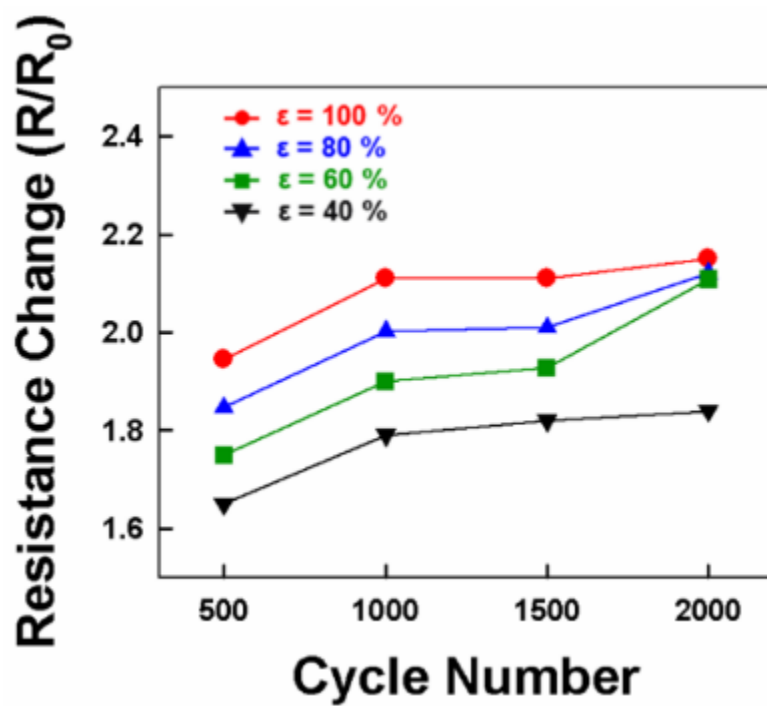
Figure S13. Resistance change of (TB-Au NP/TA)$_n$-coated PDMS. Resistance change (R/R_0) as a function of cycle number for (TB-Au NP/TA)$_{15}$-PDMS for different strains (%).

(a)

(b)
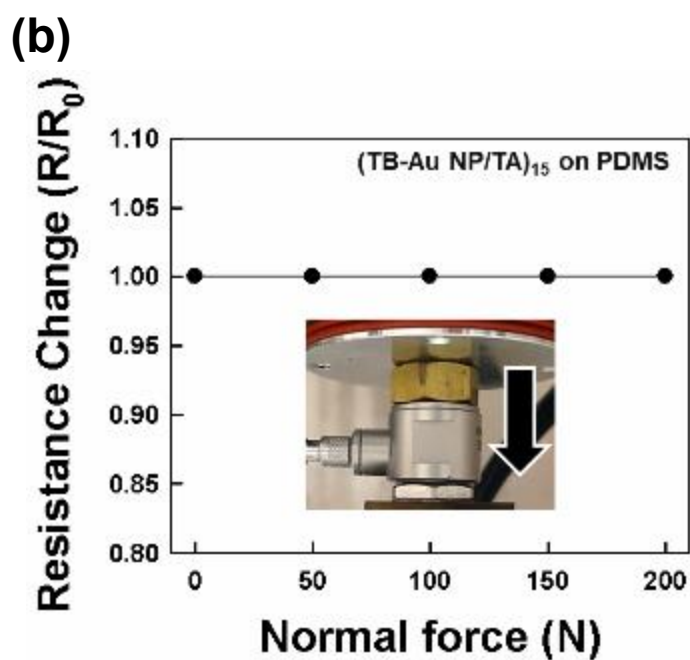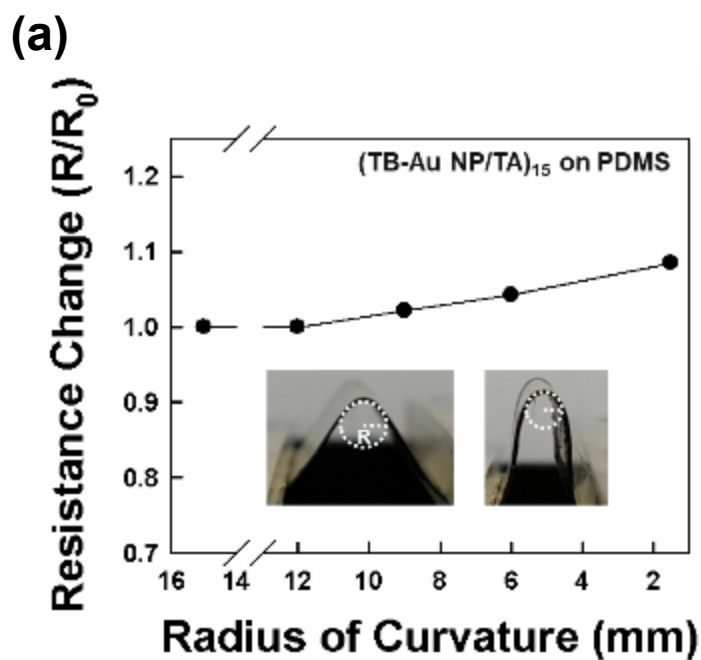
Figure S14. Electrical stability of the wrinkled elastomeric electrode. Electrical stability of approximately 500 μm-thick (TB-Au NP/TA)$_{15}$-PDMS as a function of the a) bending radius and b) compressive force.
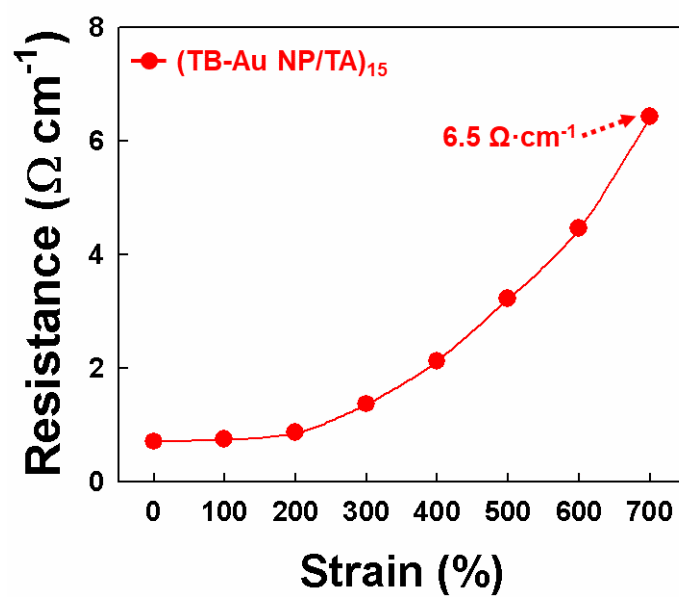
Figure S15. Resistance of a helical-structured PDMS electrode. Resistance as a function of strain for a (TB-Au NP/TA)$_{15}$-coated PDMS fiber with a helix angle of 20° and a pitch of 2.5 mm.
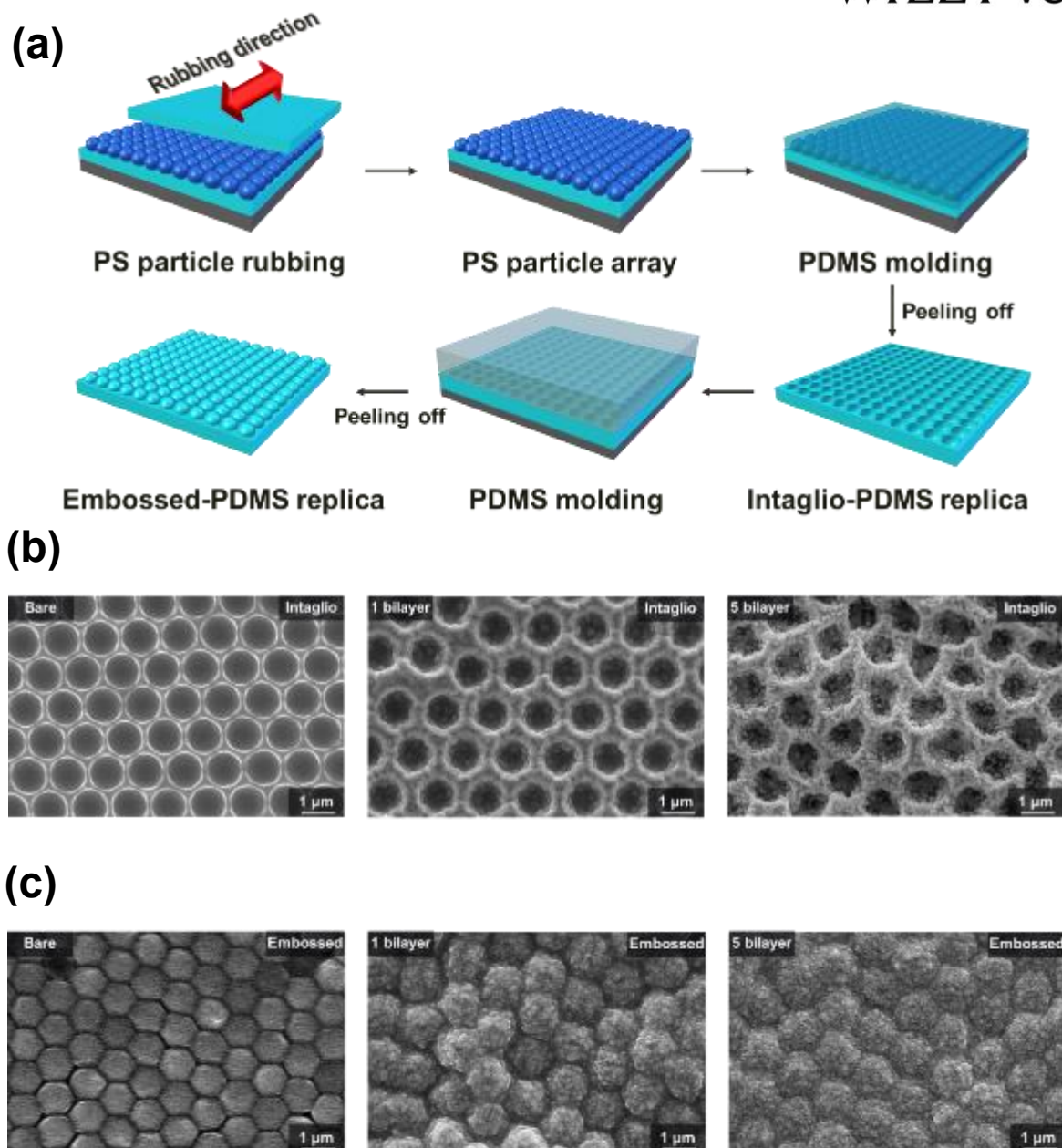
Figure S16. Preparation of PDMS electrodes with intaglio and embossed structures. a) Schematic representation of the preparation of the intaglio and embossed PDMS films. The formed films were prepared from a replica of a 1 μm-sized poly(styrene) (PS) colloid monolayer-coated substrate and intaglio-PDMS substrate, respectively. b) FE-SEM images of (TB-Au NP/TA)$_n$-coated PDMS using intaglio and c) embossed PDMS replicas.

The detailed method for the preparation of embossed and intaglio PDMS plates is as follows. First, the PDMS prepolymer mixture was spin-coated at 3000 rpm for 30 s onto a Si wafer. The formed PDMS-coated substrates were then cured at 80 °C for 5 hours. After curing, dry powder composed of negatively charged colloids with a diameter of 1 μm was placed onto the PDMS-coated Si wafer and mechanically rubbed with the other PDMS-coated

substrate. This mechanical rubbing process transferred the colloids to the PDMS-coated substrates, resulting in the formation of hexagonally packed colloidal arrays. The doctor-blade process was then used after pouring the PDMS prepolymer mixture (PDMS prepolymer: cross-linker agent = 10:1, w/w) into the PS colloidal monolayer-coated PDMS template. The thickness of the mold used for doctor-blading was approximately 500 μm. Therefore, the total thickness of the resultant PDMS films was fixed at this value. The films were thermally cured at 150 °C for 40 minutes. The cured PDMS film was carefully peeled from the PDMS template and then soaked in acetone for 24 hours to completely remove the residual PS colloids adsorbed onto the surface of the detached PDMS films.

After this etching process, the triboelectric PDMS replica with the intaglio (or microporous) structure was obtained. A triboelectric PDMS replica with an embossed structure was then prepared using the intaglio PDMS replica instead of hexagonally packed PS colloid-coated substrates. First, tri-chloro(1H,1H,2H,2H-perfluorooctyl)silane was coated onto the intaglio PDMS template, and the PDMS prepolymer mixture was subsequently poured onto the template surface (this surface treatment allows the facile detachment of the embossed PDMS replica from the intaglio PDMS template). After this step, all experimental procedures, including curing, film detachment, etching, and drying processes, for embossed PDMS were identical to those for intaglio PDMS.
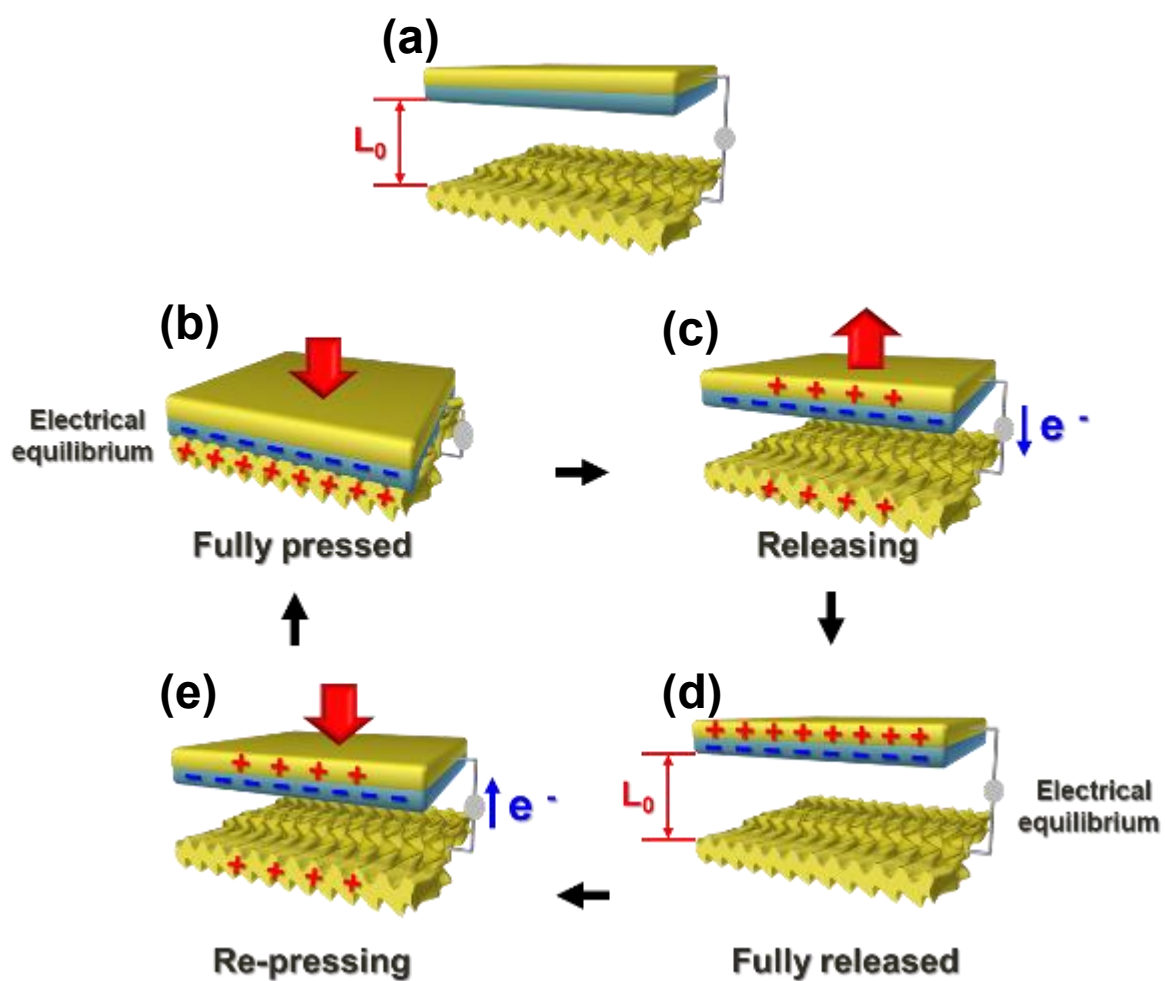
(a)

(b)

(c)

(d)

Pushing
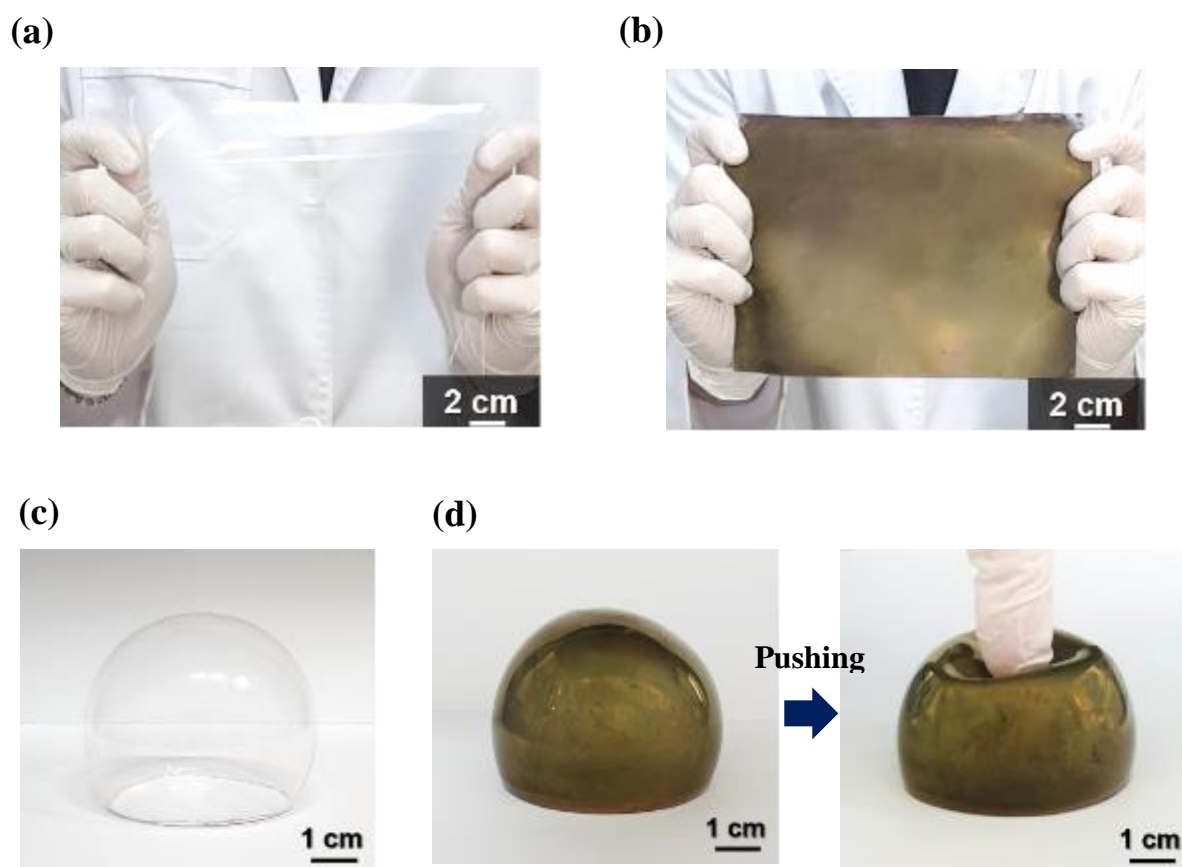
Figure S17. Photographic images of (a) bare PDMS elastomer (19.5 cm x 14.5 cm) and (b) (TB-Au NP/TA)$_n$-multilayer-coated PDMS elastomer, (c) the bare PDMS elastomer with curved shape, and (d) the (TB-Au NP/TA)$_2$-PDMS elastomer with curved shape.
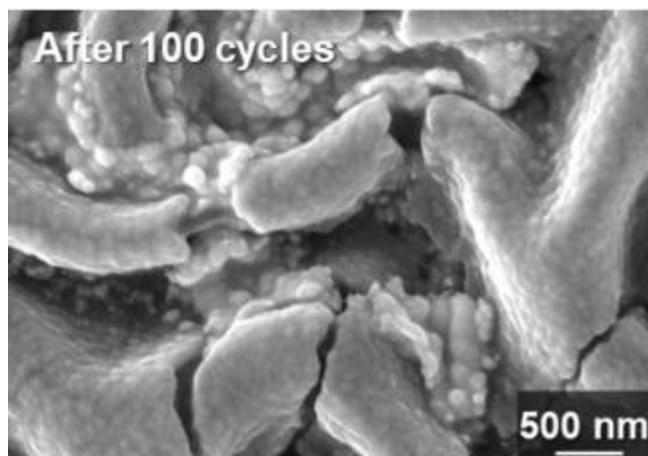
Figure S18. FE-SEM image of (TB-Au NP/TA)$_{15}$-PDMS after 100 peeling cycles

Figure S19. Schematic representation of the triboelectric mechanism of TENGs. a) Initial state without an external compressive force. b) Intimate contact between the PDMS film (top) and the elastic electrode (bottom) under a compressive force. c) Separation of the elastic electrode and PDMS film after the removal of the external compressive force. d) Recovery of the initial separation length (L_0). e) Decrease in separation length under a reapplied compressive force.
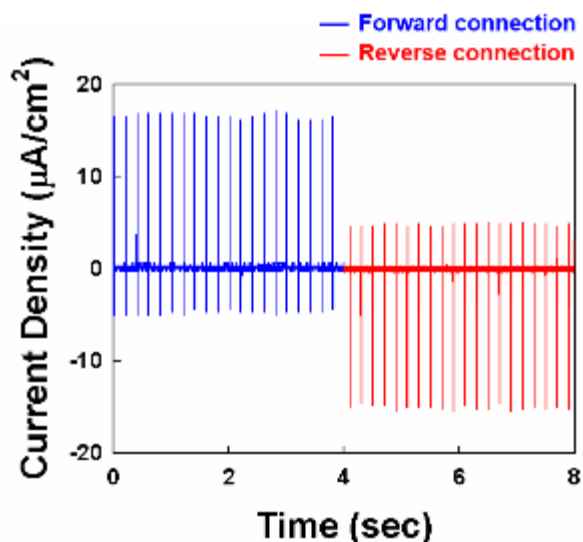
(a)
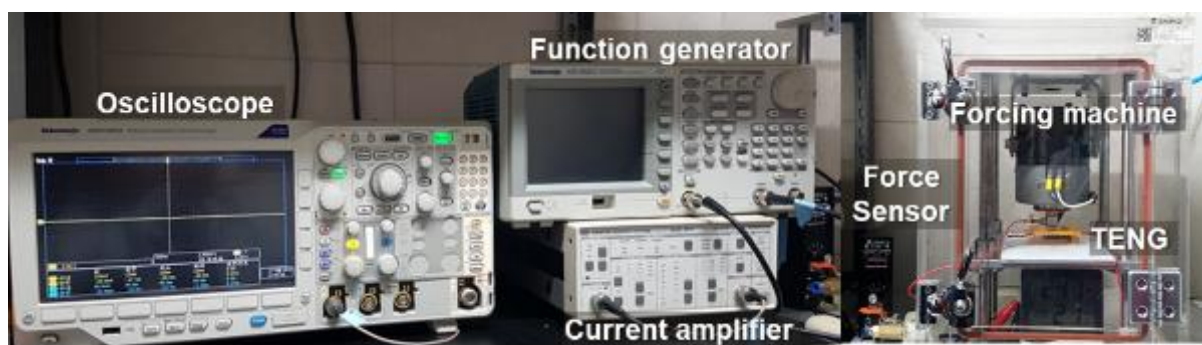
(b)
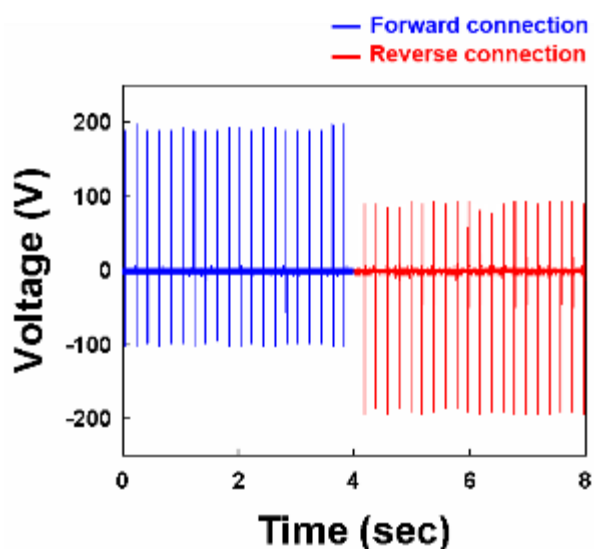
(c)

Figure S20. Triboelectric measurement of (TB-Au NP/TA)$_n$ multilayer-based TENG devices. a) Photograph of the apparatus for measuring the electrical output of (TB-Au NP/TA)$_n$ multilayer-based TENGs. b) Switching polarity tests of output voltages and c) current densities of (TB-Au NP/TA)$_n$ multilayer-based TENGs under an external compressive force of 90 N (frequency of 5 Hz). These polarity-switching tests revealed that the electric outputs of the elastomeric electrode/flat PDMS-TENG originated from the periodic contact and separation between the elastomeric contact electrode and the PDMS plates, not from the measurement system.
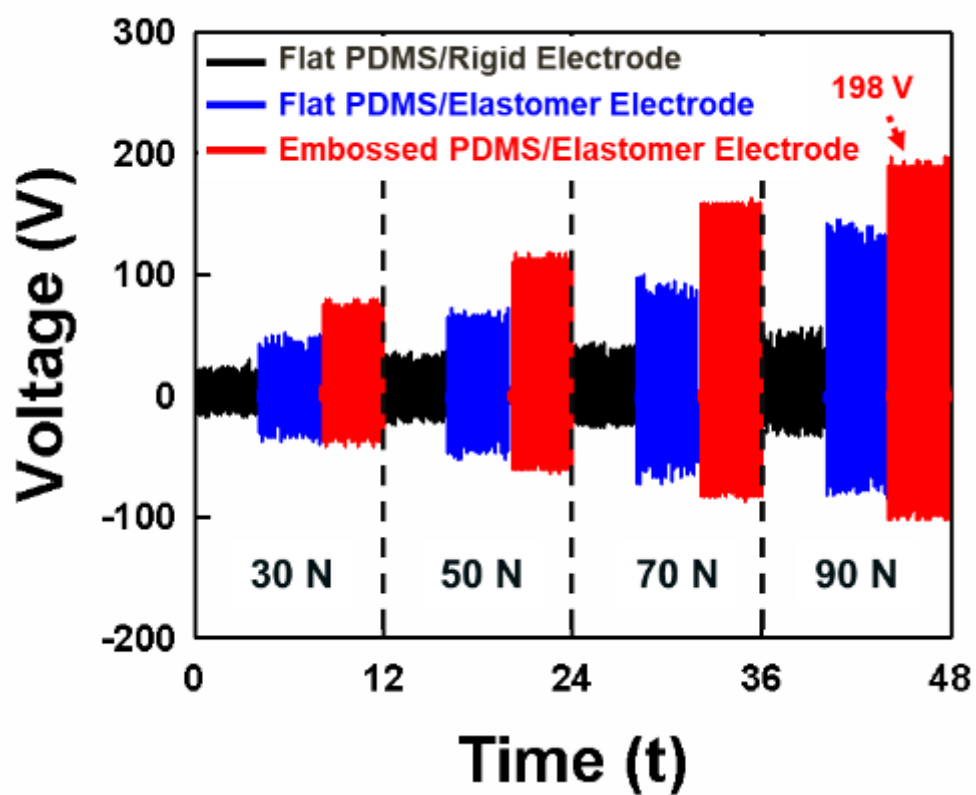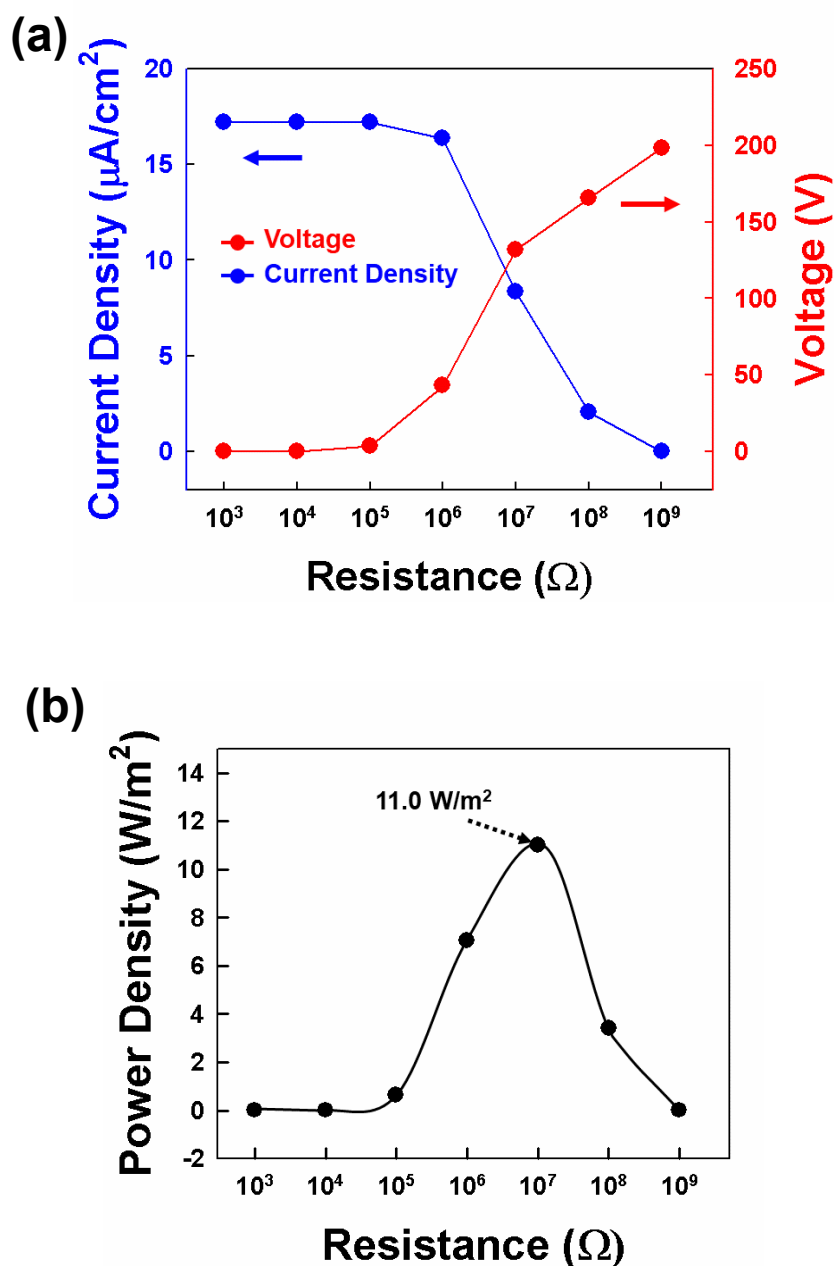
Figure S21. Output voltages of the three TENG devices as a function of compressive force.
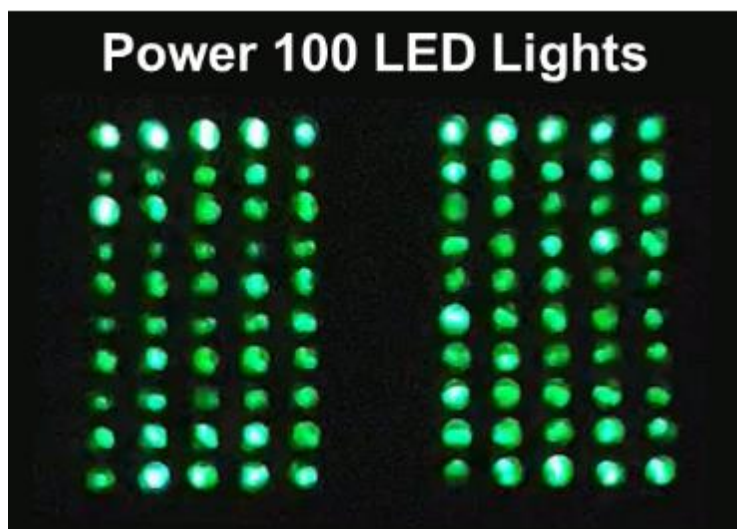
Figure S22. LEDs illuminated by all elastomer-based TENG. One hundred green LEDs illuminated by the embossed PDMS/wrinkled elastomeric electrode-based TENG device under a compressive force of 90 N.

WILEY-VCH
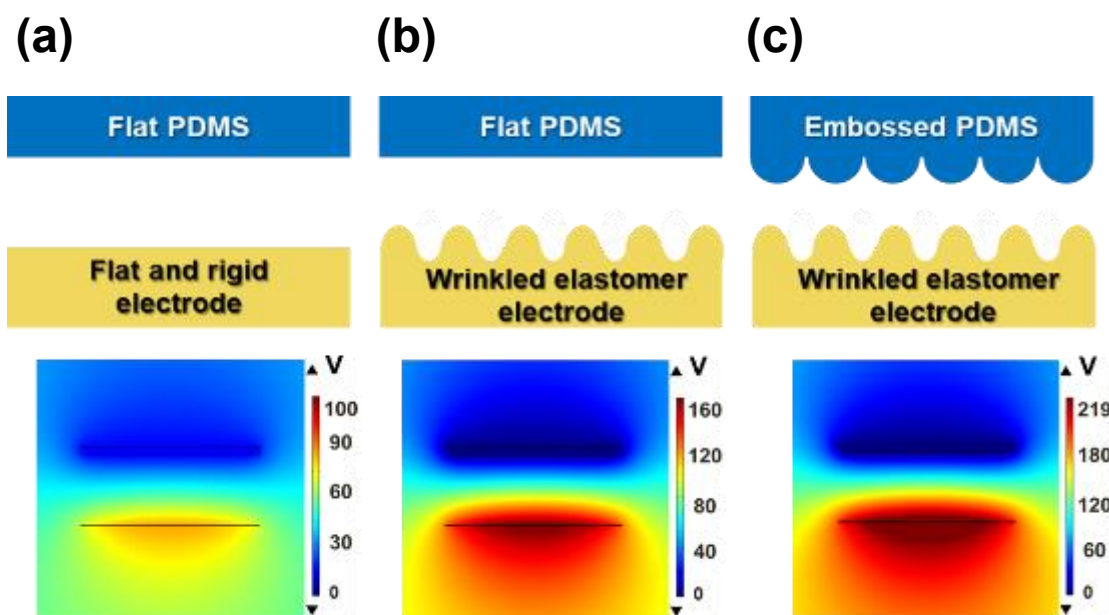
Figure S23. Triboelectric potential distribution in the different TENG electrodes. Simulation results of the triboelectric potential distribution between PDMS and the contact electrode a) (flat electrode), b) wrinkled elastomeric electrode, and c) embossed PDMS/wrinkled elastomeric electrode. Simulations were performed using COMSOL multiphysics software. For the wrinkled elastomer electrode, a wavy pattern with the wavelength of 1.6 μm was structured on the surface. The gap between the contact PDMS and the contact electrodes was fixed at 50 μm. The external pushing force was not considered in our simulation. A triboelectric charge density of two tribo-charged surfaces were assigned with ± 30 μC·m^{-2}. Additionally, flat or embossed PDMS plates with a width of 120 μm and a thickness of 5 μm were placed above the contact electrodes with the same dimensions as those of the triboelectric PDMS plates. In this case, the triboelectric potential between the PDMS film and the elastomeric electrode notably increased with increasing contact area, indicating the generation of greater triboelectric charges on its surface than on the flat PDMS surfaces of the rigid electrode-based TENG. Considering the increase in transferred charges and increase in triboelectric potential difference between the electrodes, we attribute the remarkably enhanced output performance of our wrinkled elastomeric electrode/embossed PDMS-based TENG to the increase in triboelectric surface area for charge generation (by the embossed PDMS) and transfer (by the wrinkled elastomeric electrode), as well as the increased capacitance change of the embossed PDMS plate under periodic compression and release.

Figure S24. Electric output of TENGs as a function of external resistance. a) Output voltages and current densities of the embossed PDMS/wrinkled elastomeric electrode-based TENG device under a compressive force of 90 N. b) Power densities of the embossed PDMS/wrinkled elastomeric electrode-based TENG device as a function of resistance under a compressive force of 90 N.

Figure S25. LEDs illuminated by all-elastomer-based TENGs using finger force. Photograph

showing 30 LEDs illuminated by finger tapping on an all-elastomer-based TENG.

Referneces

[S1] J. Zhang, Y. Chen, M. A. Brook, *Langmuir* **2013,** *29*, 12432.

[S2] H. Sun, *J. Phys. Chem. B* **1998**, *102*, 7338.

[S3] A. A. Samoletov, C. P. Dettmann, M. A. J. Chaplain, *J. Stat. Phys.* **2007**, *128*, 1321.

[S4] M. Parrinello, A. Rahman, *J. Appl. Phys.* **1981**, *52*, 7182.